Title

A 13C/31P surface coil to visualize metabolism and energetics in the rodent brain at 3 Tesla

Authors

Vaidya, Manushka V

Zhang, Bei

Hong, DongHyun

et al.

Publication Date

2022-10-01

DOI

10.1016/j.jmr.2022.107286

Peer reviewed

HHS Public Access

Author manuscript

J Magn Reson. Author manuscript; available in PMC 2023 October 01.

Published in final edited form as:

J Magn Reson. 2022 October ; 343: 107286. doi:10.1016/j.jmr.2022.107286.

A $^{13}C/^{31}P$ surface coil to visualize metabolism and energetics in the rodent brain at 3 Tesla

Manushka V. Vaidya[1], **Bei Zhang**[2], **DongHyun Hong**[1], **Ryan Brown**[3], **Georgios Batsios**[1], **Pavithra Viswanath**[1], **Jan Paska**[3], **Gerburg Wulf**[4], **Aaron K. Grant**[5], **Sabrina Ronen**[1], **Peder Larson**[1]

[1)]Department of Radiology and Biomedical Imaging, University of California San Francisco, San Francisco, CA, USA

[2)]Advanced Imaging Research Center, UT Southwestern Medical Center, Dallas, TX, USA

[3)]Center for Advanced Imaging Innovation and Research, and Center for Biomedical Imaging, Department of Radiology, New York University School of Medicine, New York, NY, USA

[4)]Department of Hematology-Oncology, Beth Israel Deaconess Medical Center, Boston, MA, USA

[5)]Department of Radiology, Beth Israel Deaconess Medical Center, Boston, MA, USA

Abstract

PURPOSE: We constructed a $^{13}C/^{31}P$ surface coil at 3 T for studying cancer metabolism and bioenergetics. In a single scan session, hyperpolarized ^{13}C-pyruvate MRS and ^{31}P MRS was carried out for a healthy rat brain.

METHODS: All experiments were carried out at 3 Tesla. The multinuclear surface coil was designed as two coplanar loops each tuned to either the ^{13}C or ^{31}P operating frequency with an LCC trap on the ^{13}C loop. A commercial volume proton coil was used for anatomical localization and $\boldsymbol{B_0}$ shimming. Single tuned coils operating at either the ^{13}C or ^{31}P frequency were built to evaluate the relative performance of the multinuclear coil. Coil performance metrics consisted of measuring Q factor ratio, calculating system input power using a single-pulse acquisition, and acquiring SNR and flip angle maps using 2D CSI sequences. To observe *in vivo* spectra, a bolus of hyperpolarized [1-^{13}C] pyruvate was administered via tail vein. *In vivo* ^{13}C and endogenous ^{31}P spectra were obtained in a single scan session using 1D slice selective acquisitions.

RESULTS: When compared with single tuned surface coils, the multinuclear coil performance showed a decrease in Q factor ratio, SNR, and transmit efficiency. Flip angle maps showed adequate flip angles within the phantom when the transmit voltage was set using an external phantom. Results show good detection of ^{13}C labeled lactate, alanine, and bicarbonate in addition to ATP from ^{31}P MRS.

CONCLUSIONS: The coil enables obtaining complementary information within a scan session, thus reducing the number of trials and minimizing biological variability for studies of metabolism and bioenergetics.

CORRESPONDING AUTHOR: Manushka Vaidya (manushka@gmail.com).

INTRODUCTION:

Advances in cancer drug treatments include the development of drugs that target the altered metabolic pathways of tumors [1,2]. 13-Carbon (^{13}C) Hyperpolarized Magnetic Resonance Spectroscopic Imaging (MRSI) has become a valuable tool in cancer imaging, because it allows for visualizing real-time changes in metabolic pathways in response to treatment [3]. As opposed to other imaging modalities such as FDG-PET, which can only measure the uptake of glucose, hyperpolarized ^{13}C MRSI has particularly gained momentum, because it allows for imaging downstream metabolites of the original injected ^{13}C labeled substrate [4,5]. The dynamic imaging technique also allows for quantifying the change in downstream metabolites over time, allowing for the calculation of kinetic exchange rates between metabolites like pyruvate and lactate as potential indicators of the aggressiveness of the tumor [6]. Real time visualization of tumor metabolic changes can therefore be used to assess the efficacy of the treatment in patients [7–9], and mechanistically understand changes in tumor metabolism in animal models [10–13].

A combined ^{13}C and phosphorus (^{31}P) study would be useful, especially for cancer studies, since phosphorus spectroscopy allows for quantifying metabolites such as ATP to investigate the bioenergetics of the tumor[14]. Such a study could allow for visualizing changes in or preference of oxidative versus non-oxidative metabolic pathways using ^{13}C spectroscopy and tumor cell viability using ^{31}P spectroscopy. The complementary information from ^{13}C and ^{31}P spectroscopy has been utilized in a wide variety of other metabolic studies. For example, in a cardiac metabolism study, it was demonstrated that ^{13}C MR spectroscopy was more sensitive to flow induced changes than ^{31}P measurements of energy containing phosphates and pH [15]. A hepatic metabolism study utilized ^{13}C and ^{31}P NMR to study diabetic and healthy rats [16]. Phosphocreatine from ^{31}P NMR studies and the downstream metabolic products of ^{13}C-glucose was compared in a differentiated and dedifferentiated rat hepatoma cell line [17]. Such studies often require separate radiofrequency (RF) coils for either ^{13}C or ^{31}P, requiring separate scanning sessions that potentially introduce biological variability.

Magnetic Resonance Imaging or Spectroscopy of different nuclei in the same scan session is possible using multinuclear RF coils. To achieve a dual resonating RF coil structure, several coil design strategies exist. The earliest method incorporated a trap circuit, consisting of an inductor and capacitor, in series with the tuning capacitor of the coil [18]. Such structures can suffer from poor coil sensitivity, since there is no way to block currents on the coil that are induced at the higher operating frequency [19]. Alternatively, separate coils each tuned to a single frequency can be used in combination, with a trap circuit on the lower frequency element to block currents induced at the higher frequency [19,20]. Other strategies to achieve multinuclear resonating elements include a transformer coupled circuit approach for either surface or birdcage coils, constructing a birdcage coil with four end rings instead of two, or adjusting the values of alternate capacitors on the end rings of a birdcage coil [20]. Design considerations are often a balance between the application of interest, spatial $\boldsymbol{B}_1$ profile, and adequate SNR.

A majority of the ^{13}C hyperpolarized work on animal models has been carried out using multinuclear volume coils [21]. ^{13}C surface coils for localized excitation and reception in animal models have been used either in conjunction with a volume proton coil [22,23], or designed as multinuclear surface elements with both $^{1}H/^{13}C$ frequencies [24]. For hyperpolarized ^{13}C studies on human subjects, single tuned ^{13}C coil-arrays with transmission and reception capability have been used in conjunction with the ^{1}H body coil of the scanner [25], and more recently, a dual-tuned $^{13}C/^{1}H$ head array at high field was built [26]. For phosphorus spectroscopic studies, coil-arrays targeting specific applications have been built [27–29]. For example, for investigating liver malignancies in humans, a dual-tuned $^{31}P/^{1}H$ coil was designed and constructed with one ^{1}H and one ^{31}P transmit coil and four ^{31}P receive elements [30]. To study neurodegenerative diseases in the human brain, an eight-channel degenerate birdcage phosphorus module with a nested proton module was constructed at 7 T [31]. Dedicated multinuclear coils for other X-nuclei studies such as sodium [20,32–36] and fluorine imaging [37–39] have also been designed. Often these coils have been built with a proton and X-nucleus channel, where the proton channel was used for anatomical localization and $\boldsymbol{B}_0$ shimming.

The ability to acquire from more than two nuclei with dedicated multinuclear RF coils has been explored for various applications. Early work demonstrated the use of a quadruple tuned surface coil for ^{19}F, ^{23}Na, ^{1}H, and ^{31}P MR spectroscopy for cerebral blood flow measurements in a cat brain [40], and a triple nuclear study ($^{1}H/^{31}P/^{23}Na$) used a triple tuned two-turn surface coil and a double tuned coil ($^{31}P/^{23}Na$) for studying brain metabolism during seizures in cats [41]. In humans, a commercial triple tuned surface coil ($^{1}H/^{13}C/^{31}P$) was used [42], and more recently, a quintuple-tuned coil ($^{1}H/^{19}F/^{31}P/^{23}Na/^{13}C$) at 7 T was designed for whole brain spectroscopic imaging [43].

To study energetics and metabolism in a single setting, we constructed a multinuclear $^{13}C/^{31}P$ transmit/receive surface coil. A commercial ^{1}H volume coil was used in conjunction with the multinuclear coil for anatomical localization and $\boldsymbol{B}_0$ shimming. We studied the feasibility of this design by characterizing the coil performance and imaging a healthy rat brain.

METHODS:

Experiments were carried out on a 3 T animal MRI scanner (Biospec, Bruker, Billerica MA), and animal experiments were done in accordance with the IACUC protocol. The transmit/receive $^{13}C/^{31}P$ coil (Fig. 1A) was constructed such that an inner loop with 3 cm diameter was tuned to 51.65 MHz (^{31}P frequency) and a concentric outer loop with 5 cm diameter was tuned to 32.09 MHz (^{13}C frequency). Both were tuned and matched to 50 Ohms on the bench using a 30 % saline phantom (50 mL). An “LCC” trap circuit consisting of a capacitor in parallel with a capacitor and inductor [19] on the ^{13}C coil decoupled the two channels of the multinuclear coil. The LCC component values were selected to block currents at the ^{31}P frequency and form a 446 pF capacitor at the ^{13}C frequency: $C_{parallel}$ = 94 pF, C_{series} = 82 pF, L_{series} = 206 nH. As the coil detuned inside the scanner and ^{1}H resonator, the tune and match capacitors were then adjusted so that the coil elements resonated at the respective center frequency when positioned inside the scanner and ^{1}H resonator. Either the

^{13}C or ^{31}P channel was connected to the X-nucleus channel on the scanner, while the other channel was terminated with a 50 Ohm load. The scanner's inbuilt broadband preamplifiers and transmit/receive switches were used.

To evaluate the relative performance of the dual tuned coil, separate single tuned coils were constructed, which matched the size of the ^{13}C and ^{31}P loops on the multinuclear coil (Fig. 1B). The tuning and matching of the single tuned coils (Fig. 1B) were adjusted using variable capacitors to closely match the S_{11} characteristics of the multinuclear coil when positioned inside the scanner (S_{11}<= 22.1 %) for all phantom evaluations. Anatomical or phantom localization and $\boldsymbol{B}_0$ shimming were carried out using a volume proton (^1H) coil (72 mm diameter, Bruker, MA). A coil configuration for changing between the ^1H, ^{13}C, and ^{31}P channels was set up in ParaVision 6.0.1.

Phantom evaluations:

For adjusting center frequency and system reference power for both channels, a spherical phantom (6.65 M urea-^{13}C (99 atom % ^{13}C), 3.03 M diethyl(2-oxopropyl) phosphonate, doped with 12uLMagnevist in a total volume of 1.2mL) was positioned at the center of the coil (Fig. 1A). Diethyl(2-oxopropyl) phosphonate was specifically chosen so that its phosphorus spectrum does not overlap with *in vivo* phosphorus metabolites. The optimal system reference power for a 90 degree flip angle was calculated using the small spherical phantom positioned at the center of the coil. The multinuclear coil was loaded with the saline phantom for all measurements. The reference power required to obtain a 90 degree flip angle was calculated by varying the power for a series of single pulse acquisitions, finding the power corresponding to no signal, i.e. for a 180 degree flip angle, and dividing by four to obtain the power required to obtain a 90 degree flip angle.

To characterize the performance of the coils spatially, SNR and flip angle maps were measured. The coils were loaded with a phantom consisting of ^{13}C-urea and sodium phosphate (55mL: 0.92 M Sodium phosphate, 1.39 M ^{1}Urea-^{13}C (99 atom % ^{13}C), 60 uL Magnevist). A small spherical phantom filled with H_2O was placed at the center of the coil for positioning the coil at the isocenter of the scanner. A 2D CSI sequence (flip angle = 90 degrees, slice thickness = 10 mm, matrix size = 16×16, FOV = 64 × 64 mm^2, TE = 5 ms, TR = 1s, averages = 2) was used to obtain spectroscopic images and a FLASH sequence (flip angle = 30 degrees, slice thickness = 10 mm, matrix size = 128 × 128, FOV = 64 × 64 mm^2, TE = 4 ms, TR = 100 ms, averages = 3) was used to acquire background reference proton images. Note that the spherical phantom containing water was used for localization purposes only, whereas the spherical phantom consisting of urea and diethyl phosphonate used in conjunction with the saline phantom was used for power calibration. As the system reference power was calculated using the urea and diethyl phosphonate phantom positioned at the center of the coil, the flip angle used in the 2D CSI sequence would be for a location at the center of the coil's plane. The SNR was calculated voxel-by-voxel by dividing the peak absolute signal by the standard deviation of the real part of the first voxel, corresponding to a region outside of the imaging object. The same 2D CSI sequence was used for calculating flip angle maps using a double angle method [44] acquired with 90 and 45 degree flip angles. For the flip angle maps, thresholds were applied to avoid calculating

flip angle values in regions of low SNR. Thresholds were kept constant for each nucleus. Based on the background proton images, masks were applied to both the SNR and flip angle maps. Data analysis was done in MATLAB (Mathworks, 2019).

Bench tests:

The Quality factor (Q) ratio ($Q_{unloaded}/Q_{loaded}$) was measured for all coils, and for the case with the LCC trap circuit replaced by a capacitor with effective capacitance for the ^{13}C channel. For each case, three sets of measurements were taken and then averaged to find $Q_{unloaded}$, Q_{loaded}, and the Q ratio. The predicted SNR efficiency $\left(SNR\ efficiency = \sqrt{1 - \frac{Qloaded}{Qunloaded}}\right)$ was calculated from the Q ratio [45].

Rat imaging:

For *in vivo* experiments (Fig. 1C), anatomical images (RARE sequence: flip angle = 90 degrees, TE = 12 ms, RARE factor = 8, TR = 2512.04 ms, averages = 4, matrix size = 192 × 192, FOV = 60 × 60 mm^2, slices = 20, slice thickness = 1 mm) were acquired followed by local $\boldsymbol{B}_0$ shimming within the whole head using the proton volume coil. System power calibration was carried out on the carbon channel and the phosphorus channel using the spherical phantom consisting of urea and diethyl phosphonate positioned at the center of the coil.

To visualize the conversion of pyruvate to its downstream metabolic products *in vivo*, a bolus of hyperpolarized [1-^{13}C] pyruvate (Testbed polarizer, Oxford Instruments, Oxfordshire UK) was administered to a healthy rat via tail vein. Slice selective spectroscopic sequences were used to obtain ^{13}C (flip angle = 30 degrees, slice thickness = 10 mm, TR = 3s, repetitions = 64, spectral points = 2048, spectral bandwidth = 6421.23 Hz) and ^{31}P (flip angle = 60 degrees, slice thickness = 15 mm, TR = 4s, averages = 256, spectral points = 2048, spectral bandwidth = 6421.23 Hz) spectra through the brain during a single scan session. Data were reconstructed in Mnova (MestReNova, 14.1.0).

RESULTS:

The Q ratio measurements predicted the SNR efficiency of the ^{13}C channel of the multinuclear coil to be 27.3 % lower than the single tuned coil (Table). On the other hand, the ^{31}P SNR efficiency was predicted to be 6.53 % lower for the multinuclear coil compared to the single tuned coil (Table).

The carbon channel of the multinuclear coil required 81 % higher transmit power, compared to the single tuned coil (Multinuclear coil ^{13}C channel: 0.95 W, Single tuned ^{13}C coil: 0.525 W), to achieve a 90 degree flip angle at the center of the coil, demonstrating a reduction in transmit efficiency. No significant difference in power was observed for the phosphorus channel when compared to the respective single tuned coil (Multinuclear coil ^{31}P channel: 0.07 W, Single tuned ^{31}P coil: 0.07 W). SNR maps (Fig. 2) showed an expected field distribution within the phantom for all coils, with decaying SNR away from the position of the coil. The multinuclear coil showed a reduced mean SNR, with a region of interest over the entire imaged slices, for both channels as compared to their corresponding individually

tuned coils (Carbon: - 36.27 % axial, - 38.03 % sagittal; Phosphorus: - 31.44 % axial, - 17.83 % sagittal). Flip angle maps (Fig. 3) for the multinuclear coil showed that the expected nominal flip angle of 45 degrees was achievable at a location within the phantom for all coils when the system power was calibrated using the small urea/diethyl(2-oxopropyl) phosphonate phantom positioned at the center of the coil. Proton images of the phantom showed a signal drop, likely caused due to destructive interference between the ^{1}H resonator and the surface coils (Fig. 4).

In vivo experiments using the multinuclear coil for a rat brain showed clear phosphorus and carbon containing metabolites (Fig. 5). In particular, the phosphorus spectrum in the rat brain showed phosphocreatine and ATP peaks. Inorganic phosphate, phosphomonoesters, and phosphodiesters were also observed (Fig. 5B). The hyperpolarized carbon spectrum summed over 18 s to 1 minute after injection showed the downstream metabolic products of ^{13}C-pyruvate, namely lactate, alanine, and bicarbonate (Fig 5C). Lactate appeared in the initial frames of the dynamic carbon spectra (Fig. 6), while alanine was observed in later frames.

DISCUSSION:

This work demonstrates the implementation and feasibility of a $^{13}C/^{31}P$ surface coil in combination with an existing volume ^{1}H coil to visualize metabolism, energetics, and anatomy in a single scan session.

A nested loop design for the $^{13}C/^{31}P$ coil (Fig. 1) was chosen over a single loop design with two resonances to include an LCC trap on the lower frequency coil, which has been shown to improve coil sensitivity [19]. Coil losses, introduced by the additional lumped elements on the LCC trap circuit, likely contributed to the lower transmit efficiency, SNR (Fig. 2), and Q ratio (Table) of the carbon channel. Previous work on a 6 cm loop at 74.7 MHz showed approximately 5 % decrease in SNR for a multinuclear coil with a LCC trap circuit compared to a single tuned coil [19]. For the coil used in this work (5 cm loop at 32.1 MHz), the low operating frequency and small sample loading [46] likely resulted in a larger decrease in SNR (Fig 2, Table) of the carbon channel with the LCC trap circuit compared to the single tuned reference coil. One strategy to improve SNR could be a smaller loop size for the ^{13}C channel comparable to the ^{31}P channel (3 cm loop) for the target volume of the rat brain, since the optimum loop diameter for maximum SNR is approximately equal to the sample depth [47]. Our results also demonstrated that replacing the LCC trap circuit by a capacitor with effective capacitance improved the Q ratio and SNR efficiency of the ^{13}C channel (Table). The result suggests that the LCC trap circuit contributed to coil losses that resulted in a lower SNR. Previous work showed higher SNR losses for increasing values of trap inductance [19]. Therefore, a lower trap inductance on the ^{13}C channel may improve SNR performance, but with a possible tradeoff of a lower blocking amplitude. A smaller sized loop for the ^{13}C channel would be further advantageous, since the loop would require larger capacitor values, which would translate to a smaller minimum trap inductance, as given by Eq. 3 in ref [19], and consequently translate to lower coil losses and higher SNR. Additional strategies to improve the SNR could include designs without the LCC trap circuit. For example, using an in-line switch on the ^{13}C coil. Other designs to consider

would be orthogonal coil elements that are naturally decoupled and do not require a LCC trap circuit [48], cryo-coils with inherent low coil losses [49], or alternative coplanar designs with an outer loop tuned to the proton frequency and interchangeable inner loops tuned to either the carbon or phosphorus resonance frequency [17].

The flip angle maps (Fig. 3) for all coils show that setting the input transmit voltage using an external small phantom allowed for the expected flip angle within the phantom, suggesting that the set-up can be used for power calibration when imaging *in vivo*. Both SNR (Fig. 2) and flip angle maps (Fig. 3) demonstrated a decay in signal intensity and flip angle away from the coil, as expected for a surface coil [50,51]. Although the surface coil design of the multinuclear $^{13}C/^{31}P$ coil was chosen to allow for future imaging of subcutaneous tumors, studies requiring homogeneous flip angles such as metabolic kinetic rate studies [6] could benefit from a multinuclear quadrature birdcage design [21].

Our results showed a small signal drop in ^{1}H phantom images (Fig. 4), and no visible signal drop for the *in vivo* anatomical image (Fig. 5) near the position of the coil. Therefore, a trap circuit, which would have further contributed to loss in SNR, was not used to reduce coupling between the multinuclear surface coil and the proton volume coil used in conjunction. Cable traps, used to minimize cable currents, were not included, although the board was originally designed to accommodate them, since the proximity of the traps might have introduced additional coupling between neighboring traps and the coil.

Despite the lower transmit efficiency and SNR of the multinuclear coil as compared to the single tuned coils, *in vivo* carbon and phosphorus metabolites were clearly observed with adequate signal and resolution (Figs. 5 and 6). Downstream metabolites of hyperpolarized [1-^{13}C] pyruvate with inherent low concentration *in vivo* such as alanine and bicarbonate were also observed (Fig. 5C). Because of the 1D slice selective acquisition that included the brain and the adjoining tissue, it is unclear whether downstream metabolic products of [1-^{13}C] pyruvate such as lactate and bicarbonate originated in the brain (Fig. 5A). Therefore, future studies would benefit from fast 2-D sequences like Echo planar spectroscopic imaging [52]. In the same scanning session, the observation of phosphorus metabolites, in particular, ATP (Fig. 5B), demonstrated the feasibility of probing the bioenergetics of the tissue along with metabolism. As other phosphorus metabolites such as inorganic phosphate and phosphocreatine were also observed (Fig. 5B), the pH of the tumor microenvironment [14] in addition to the bioenergetics and metabolism could be studied in future work. Quantification of the observed *in vivo* phosphorus metabolites could be carried out in future studies using the external phantom, which was used primarily for power calibration in our study.

Our current experimental set-up at 3T required a 17-minute-long acquisition of 256 averages for acquiring the phosphorus spectrum. Higher field strength would allow for greater SNR [53,54], reducing acquisition time for a more real-time assessment of cell viability, and allow for visualizing metabolites with inherent low concentration. However, 3T is advantageous for hyperpolarized ^{13}C agents because they have longer T_1 relaxation times at this field strength and do not benefit from the higher thermal polarization at higher field strengths. Other modifications to consider would be the implementation of a switch

to change between the ^{31}P and ^{13}C channels towards a more streamlined simultaneous acquisition.

CONCLUSIONS:

The $^{13}C/^{31}P$ multinuclear coil designed and tested in this study, was used in combination with a commercial ^{1}H volume coil to visualize metabolism, energetics, and anatomy. A nested loop design for the $^{13}C/^{31}P$ coil was chosen over a single loop design to include an LCC trap on the lower frequency coil, which improves coil sensitivity. Despite lower coil performance as compared to single tuned coils, downstream metabolic products of 1-^{13}C pyruvate with low concentration such as bicarbonate, as well as endogenous ^{31}P metabolites were observed for a healthy rat brain, demonstrating potential for this type of multinuclear design.

ACKNOWLEDGEMENTS:

This work was supported by NIH Training Grant T32CA151022, American Cancer Society Research Scholar Grant 18-005-01-CCE, NIH R01CA172845, NIH R01CA197254, NIH grant P41 EB013598 and P41 EB017183. The authors would like to thank Rohan Virgincar for discussions regarding creating multinuclear coil files in ParaVision.

REFERENCES:

[1]. vander Heiden MG, Targeting cancer metabolism: a therapeutic window opens, Nature Publishing Group. 10 (2011). 10.1038/nrd3504.

[2]. Martinez-Outschoorn UE, Peiris-Pagès M, Pestell RG, Sotgia F, Lisanti MP, Cancer metabolism: a therapeutic perspective, NATURE REVIEWS | CLINICAL ONCOLOGY. 14 (2016). 10.1038/nrclinonc.2016.60.

[3]. Ardenkjaer-Larsen JH, Fridlund B, Gram A, Increase in signal-to-noise ratio of > 10,000 times in liquid-state NMR, Proc Natl Acad Sci USA. 100 (2003) 10158–10163. 10.1073/pnas.1733835100. [PubMed: 12930897]

[4]. Gallagher FA, Bohndiek SE, Kettunen MI, Lewis DY, Soloviev D, Brindle KM, Hyperpolarized 13C MRI and PET: In Vivo Tumor Biochemistry, Journal of Nuclear Medicine. 52 (2011) 1333–1336. 10.2967/JNUMED.110.085258. [PubMed: 21849405]

[5]. Hesketh RL, Wang J, Wright AJ, Lewis DY, Denton AE, Grenfell R, Miller JL, Bielik R, Gehrung M, Fala M, Ros S, Xie B, Hu D, Brindle KM, Metabolism and Chemical Biology Magnetic Resonance Imaging Is More Sensitive Than PET for Detecting Treatment-Induced Cell Death-Dependent Changes in Glycolysis, (2019). 10.1158/0008-5472.CAN-19-0182.

[6]. Larson PEZ, Chen HY, Gordon JW, Korn N, Maidens J, Arcak M, Tang S, Criekinge M, Carvajal L, Mammoli D, Bok R, Aggarwal R, Ferrone M, Slater JB, Nelson SJ, Kurhanewicz J, Vigneron DB, Investigation of analysis methods for hyperpolarized 13C-pyruvate metabolic MRI in prostate cancer patients, NMR in Biomedicine. (2018). 10.1002/nbm.3997.

[7]. Aggarwal R, Vigneron DB, Kurhanewicz J, Hyperpolarized 1-[13C]-Pyruvate Magnetic Resonance Imaging Detects an Early Metabolic Response to Androgen Ablation Therapy in Prostate Cancer, Eur Urol. 72 (2017) 1028. 10.1016/J.EURURO.2017.07.022. [PubMed: 28765011]

[8]. Wang ZJ, Ohliger MA, Larson PEZ, Gordon JW, Bok RA, Slater J, Villanueva-Meyer JE, Hess CP, Kurhanewicz J, Vigneron DB, Hyperpolarized 13C MRI: State of the Art and Future Directions, Https://Doi.Org/10.1148/Radiol.2019182391. 291 (2019) 273–284. 10.1148/RADIOL.2019182391.

[9]. Woitek R, McLean MA, Gill AB, Grist JT, Provenzano E, Patterson AJ, Ursprung S, Torheim T, Zaccagna F, Locke M, Laurent M-C, Hilborne S, Frary A, Beer L, Rundo L, Patterson I, Slough R, Kane J, Biggs H, Harrison E, Lanz T, Basu B, Baird R, Sala E, Graves MJ, Gilbert FJ, Abraham JE, Caldas C, Brindle KM, Gallagher FA, Hyperpolarized 13 C MRI of Tumor

Metabolism Demonstrates Early Metabolic Response to Neoadjuvant Chemotherapy in Breast Cancer, Radiology: Imaging Cancer. 2 (2020) e200017. 10.1148/RYCAN.2020200017/ASSET/IMAGES/LARGE/RYCAN.2020200017.FIG1B.JPEG. [PubMed: 32803167]

[10]. Day SE, Kettunen MI, Gallagher FA, Detecting tumor response to treatment using hyperpolarized 13C magnetic resonance imaging and spectroscopy., Nat Med. 13 (2007) 1382–1387. 10.1038/nm1650. [PubMed: 17965722]

[11]. Chen AP, Albers MJ, Cunningham CH, Kohler SJ, Yen YF, Hurd RE, Tropp J, Bok R, Pauly JM, Nelson SJ, Kurhanewicz J, Vigneron DB, Hyperpolarized C-13 spectroscopic imaging of the TRAMP mouse at 3T - Initial experience, Magnetic Resonance in Medicine. 58 (2007) 1099–1106. 10.1002/MRM.21256. [PubMed: 17969006]

[12]. Albers MJ, Bok R, Chen AP, Cunningham CH, Zierhut ML, Zhang VY, Kohler SJ, Tropp J, Hurd RE, Yen Y-F, Nelson SJ, Vigneron DB, Kurhanewicz J, Hyperpolarized 13C Lactate, Pyruvate, and Alanine: Noninvasive Biomarkers for Prostate Cancer Detection and Grading, Cancer Research. 68 (2008) 8607–8615. 10.1158/0008-5472.CAN-08-0749. [PubMed: 18922937]

[13]. Chaumeil MM, Ozawa T, Park IW, Scott K, James CD, Nelson SJ, Ronen SM, Hyperpolarized 13C MR spectroscopic imaging can be used to monitor Everolimus treatment in vivo in an orthotopic rodent model of glioblastoma, Neuroimage. 59 (2012) 193–201. 10.1016/J.NEUROIMAGE.2011.07.034. [PubMed: 21807103]

[14]. de Graaf RA, In Vivo NMR Spectroscopy – Static Aspects, In Vivo NMR Spectroscopy. (2018) 43–128. 10.1002/9781119382461.CH2.

[15]. Weiss RG, Chacko VP, Glickson JD, Gerstenblith G, Comparative 13C and 31P NMR assessment of altered metabolism during graded reductions in coronary flow in intact rat hearts, Proc Natl Acad Sci U S A. 86 (1989) 6426–6430. 10.1073/pnas.86.16.6426. [PubMed: 2762333]

[16]. Cohen SM, Carbon-13 and phosphorus-31 NMR study of gluconeogenesis: utilization of carbon-13-labeled substrates by perfused liver from streptozotocin-diabetic and untreated rats, Biochemistry. 26 (1987) 563–572. 10.1021/bi00376a031. [PubMed: 3030411]

[17]. Ronen SM, Volk A, Mispelter J, Comparative NMR study of a differentiated rat hepatoma and its dedifferentiated subclone cultured as spheroids and as implanted tumors, NMR in Biomedicine. 7 (1994) 278–286. 10.1002/nbm.1940070605. [PubMed: 7841024]

[18]. Schnall MD, Harihara Subramanian V, Leigh JS, Chance B, A new double-tuned probed for concurrent 1H and 31P NMR, Journal of Magnetic Resonance (1969). 65 (1985) 122–129. 10.1016/0022-2364(85)90380-4.

[19]. Meyerspeer M, Roig ES, Gruetter R, Magill AW, An improved trap design for decoupling multinuclear RF coils, Magnetic Resonance in Medicine. 72 (2014) 584–590. 10.1002/mrm.24931. [PubMed: 24006123]

[20]. Wiggins GC, Brown R, Lakshmanan K, High Performance RF Coils for 23Na MRI: Brain and Musculoskeletal Applications, NMR Biomed. 29 (2016) 96. 10.1002/NBM.3379. [PubMed: 26404631]

[21]. Derby K, Tropp J, Hawryszko C, Design and evaluation of a novel dual-tuned resonator for spectroscopic imaging, Journal of Magnetic Resonance (1969). 86 (1990) 645–651. 10.1016/0022-2364(90)90043-9.

[22]. Grant AK, Vinogradov E, Wang X, Lenkinski RE, Alsop DC, Perfusion imaging with a freely diffusible hyperpolarized contrast agent, Magnetic Resonance in Medicine. 66 (2011) 746–755. 10.1002/MRM.22860. [PubMed: 21432901]

[23]. Seth P, Grant A, Tang J, Vinogradov E, Wang X, Lenkinski R, Sukhatme VP, On-target Inhibition of Tumor Fermentative Glycolysis as Visualized by Hyperpolarized Pyruvate, Neoplasia. 13 (2011) 60–71. 10.1593/NEO.101020. [PubMed: 21245941]

[24]. Cao P, Zhang X, Park I, Najac C, Nelson SJ, Ronen S, Larson PEZ, 1H-13C independently tuned radiofrequency surface coil applied for in vivo hyperpolarized MRI, Magnetic Resonance in Medicine. 76 (2016) 1612–1620. 10.1002/MRM.26046. [PubMed: 26597845]

[25]. Grist JT, Hansen ESS, Sánchez-Heredia JD, McLean MA, Tougaard R, Riemer F, Schulte RF, Kaggie JD, Ardenkjaer-Larsen JH, Laustsen C, Gallagher FA, Creating a clinical platform for carbon-13 studies using the sodium-23 and proton resonances, Magnetic Resonance in Medicine. 84 (2020) 1817–1827. 10.1002/MRM.28238. [PubMed: 32167199]

[26]. Avdievich NI, Solomakha G, Ruhm L, Henning A, Scheffler K, 9.4 T double-tuned 13C/1H human head array using a combination of surface loops and dipole antennas, NMR in Biomedicine. 34 (2021) e4577. 10.1002/NBM.4577. [PubMed: 34169590]

[27]. Goluch S, Kuehne A, Meyerspeer M, Kriegl R, Schmid AI, Fiedler GB, Herrmann T, Mallow J, Hong SM, Cho ZH, Bernarding J, Moser E, Laistler E, A form-fitted three channel 31P, two channel 1H transceiver coil array for calf muscle studies at 7 T, Magnetic Resonance in Medicine. 73 (2015) 2376–2389. 10.1002/MRM.25339. [PubMed: 25046817]

[28]. Rivera D, Kalleveen I, de Castro CA, van Laarhoven H, Klomp D, van der Kemp W, Stoker J, Nederveen A, Inherently decoupled 1H antennas and 31P loops for metabolic imaging of liver metastasis at 7 T, NMR in Biomedicine. 33 (2020) e4221. 10.1002/NBM.4221. [PubMed: 31922319]

[29]. Avdievich NI, Ruhm L, Dorst J, Scheffler K, Korzowski A, Henning A, Double-tuned 31P/1H human head array with high performance at both frequencies for spectroscopic imaging at 9.4T, Magnetic Resonance in Medicine. 84 (2020) 1076–1089. 10.1002/MRM.28176. [PubMed: 32003031]

[30]. Panda A, Jones S, Stark H, Raghavan RS, Sandrasegaran K, Bansal N, Dydak U, Phosphorus liver MRSI at 3 T using a novel dual-tuned eight-channel ^{31} P/ ^{1} H coil, Magnetic Resonance in Medicine. 68 (2012) 1346–1356. 10.1002/mrm.24164. [PubMed: 22287206]

[31]. Brown R, Lakshmanan K, Madelin G, Parasoglou P, A nested phosphorus and proton coil array for brain magnetic resonance imaging and spectroscopy, Neuroimage. 124 (2016) 602–611. 10.1016/j.neuroimage.2015.08.066. [PubMed: 26375209]

[32]. Kim JH, Moon CH, Park BW, Furlan A, Zhao T, Bae KT, Multichannel transceiver dual-tuned RF coil for proton/sodium MR imaging of knee cartilage at 3 T, Magnetic Resonance Imaging. 30 (2012) 562–571. 10.1016/J.MRI.2011.12.011. [PubMed: 22297242]

[33]. Moon CH, Kim JH, Zhao T, Bae KT, Quantitative 23Na MRI of human knee cartilage using dual-tuned 1H/23Na transceiver array radiofrequency coil at 7 tesla, Journal of Magnetic Resonance Imaging. 38 (2013) 1063–1072. 10.1002/JMRI.24030. [PubMed: 24123257]

[34]. Brown R, Madelin G, Lattanzi R, Chang G, Regatte RR, Sodickson DK, Wiggins GC, Design of a nested eight-channel sodium and four-channel proton coil for 7T knee imaging, Magnetic Resonance in Medicine. 70 (2013) 259–268. 10.1002/mrm.24432. [PubMed: 22887123]

[35]. Ianniello C, Madelin G, Moy L, Brown R, A dual-tuned multichannel bilateral RF coil for 1H/23Na breast MRI at 7 T, Magn Reson Med. 82 (2019) 1566. 10.1002/MRM.27829. [PubMed: 31148249]

[36]. Boehmert L, Kuehne A, Waiczies H, Wenz D, Eigentler TW, Funk S, von Knobelsdorff-Brenkenhoff F, Schulz-Menger J, Nagel AM, Seeliger E, Niendorf T, Cardiorenal sodium MRI at 7.0 Tesla using a 4/4 channel 1H/23Na radiofrequency antenna array, Magnetic Resonance in Medicine. 82 (2019) 2343–2356. 10.1002/MRM.27880. [PubMed: 31257651]

[37]. Chen J, Lanza GM, Wickline SA, Quantitative Magnetic Resonance Fluorine Imaging: Today and tomorrow, Wiley Interdiscip Rev Nanomed Nanobiotechnol. 2 (2010) 431. 10.1002/WNAN.87. [PubMed: 20564465]

[38]. Ruiz-Cabello J, Barnett BP, Bottomley PA, Bulte JWM, Fluorine (19F) MRS and MRI in biomedicine, NMR Biomed. 24 (2011) 114. 10.1002/NBM.1570. [PubMed: 20842758]

[39]. Ji Y, Waiczies H, Winter L, Neumanova P, Hofmann D, Rieger J, Mekle R, Waiczies S, Niendorf T, Eight-channel transceiver RF coil array tailored for ^{1}H/^{19}F MR of the human knee and fluorinated drugs at 7.0 T, NMR Biomed. 28 (2015) 726–737. 10.1002/NBM.3300. [PubMed: 25916199]

[40]. Eleff SM, Schnall MD, Ligetti L, Osbakken M, Subramanian H, Chance B, Leigh JS, Concurrent measurements of cerebral blood flow, sodium, lactate, and high-energy phosphate metabolism using 19F, 23Na, 1H, and 31P nuclear magnetic resonance spectroscopy, Magnetic Resonance in Medicine. 7 (1988) 412–424. 10.1002/mrm.1910070404. [PubMed: 3173056]

[41]. Schnall MD, Yoshizaki K, Chance B, Leigh JS, Triple nuclear NMR studies of cerebral metabolism during generalized seizure, Magn Reson Med. 6 (1988) 15–23. 10.1002/MRM.1910060103. [PubMed: 3352502]

[42]. Krebs M, Krssak M, Bernroider E, Anderwald C, Brehm A, Meyerspeer M, Nowotny P, Roth E, Waldhäusl W, Roden M, Mechanism of Amino Acid-Induced Skeletal Muscle Insulin Resistance in Humans, Diabetes. 51 (2002) 599–605. 10.2337/DIABETES.51.3.599. [PubMed: 11872656]

[43]. Dai J, van der Velden TA, Hoogduin JM, Bartel F, Meliado EF, van Uden M, Arteaga de Castro CS, Wiegers EC, Froeling M, Gosselink M, Raaijmakers AJE, Klomp DWJ, A Quintuple-Tuned RF Coil for Whole Brain Multi-Nuclei Magnetic Resonance Imaging andSpectroscopy at 7T, in: In: Proceedings of the 2021 International Society of Magnetic Resonance in Medicine, 2021: p. 0178.

[44]. Stollberger R, Wach P, McKinnon G, Justich E, Ebner F, Rf-field mapping in vivo, In: Proceedings of the 7th Annual Meeting of SMRM, San Francisco, CA, USA. (1988) 106.

[45]. Rudin M, In-Vivo Magnetic Resonance Spectroscopy I: Probeheads and Radiofrequency Pulses Spectrum Analysis, Springer Berlin Heidelberg, 1992.

[46]. Doty FD, Entzminger G, Kulkarni J, Pamarthy K, Staab JP, Radio frequency coil technology for small-animal MRI, (n.d.). 10.1002/nbm.1149.

[47]. Wang J, Reykowski A, Dickas J, Calculation of the Signal-to-Noise Ratio for Simple Surface Coils and Arrays of Coils, IEEE Transactions on Biomedical Engineering. 42 (1995) 908–917. 10.1109/10.412657. [PubMed: 7558065]

[48]. Alfonsetti M, Sotgiu A, Alecci M, Design and testing of a 1.5 Tesla double-tuned (1H/ 31P) RF surface coil with intrinsic geometric isolation, Measurement: Journal of the International Measurement Confederation. (2010). 10.1016/j.measurement.2010.07.003.

[49]. Kovacs H, Moskau D, Spraul M, Cryogenically cooled probes—a leap in NMR technology, Progress in Nuclear Magnetic Resonance Spectroscopy. 46 (2005) 131–155. 10.1016/J.PNMRS.2005.03.001.

[50]. Keltner JR, Carlson JW, Roos MS, Wong STS, Wong TL, Budinger TF, Electromagnetic fields of surface coil in vivo NMR at high frequencies, Magnetic Resonance in Medicine. 22 (1991) 467–480. 10.1002/MRM.1910220254. [PubMed: 1812380]

[51]. Vaidya MV, Collins CM, Sodickson DK, Brown R, Wiggins GC, Lattanzi R, Dependence of B1- and B1+ field patterns of surface coils on the electrical properties of the sample and the MR operating frequency, Concepts in Magnetic Resonance Part B: Magnetic Resonance Engineering. 46 (2016). 10.1002/cmr.b.21319.

[52]. Mulkern R. v., Panych LP, Echo planar spectroscopic imaging, Concepts in Magnetic Resonance. 13 (2001) 213–237. 10.1002/CMR.1011.

[53]. Hoult DI, Phil D, Sensitivity and Power Deposition in a High-Field Imaging Experiment, J. Magn. Reson. Imaging 12 (2000) 46–67. 10.1002/1522-2586. [PubMed: 10931564]

[54]. Collins CM, Smith MB, Signal-to-noise ratio and absorbed power as functions of main magnetic field strength, and definition of “90°” RF pulse for the head in the birdcage coil, Magnetic Resonance in Medicine. 45 (2001) 684–691. 10.1002/MRM.1091. [PubMed: 11283997]

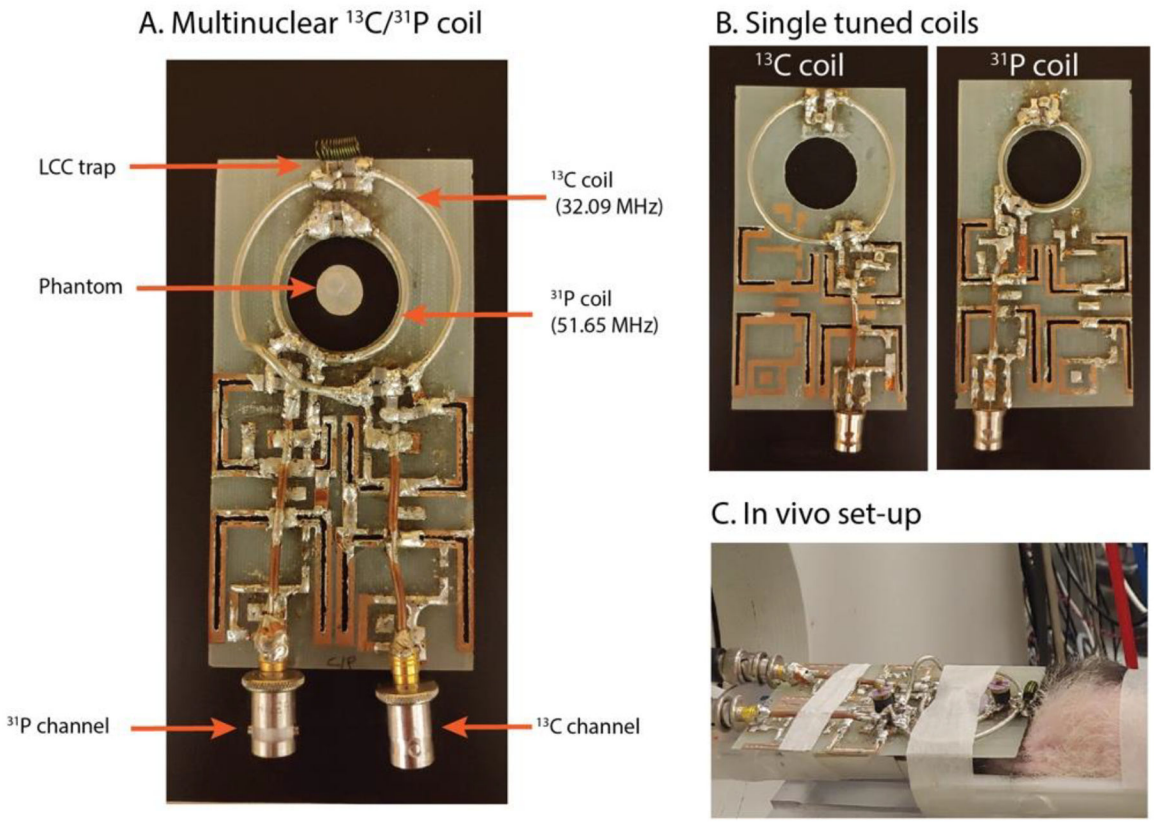

Figure 1:

Surface coils and in vivo set up. Multinuclear coil designed for metabolic and bioenergetics imaging for a rat brain at 3T is shown in A. The inner loop (3 cm diameter) was tuned to the ^{31}P frequency, and the outer loop (5 cm diameter) was tuned to the ^{13}C operating frequency. An LCC trap was included on the ^{13}C loop, and a phantom was positioned at the center of the coil for center frequency adjustment and power calibration. Single tuned coils (B) were constructed to match the diameter of either the ^{13}C loop or ^{31}P loop in the multinuclear coil (A) for evaluating coil performance. The multinuclear coil was positioned on the top of a rat head (C).

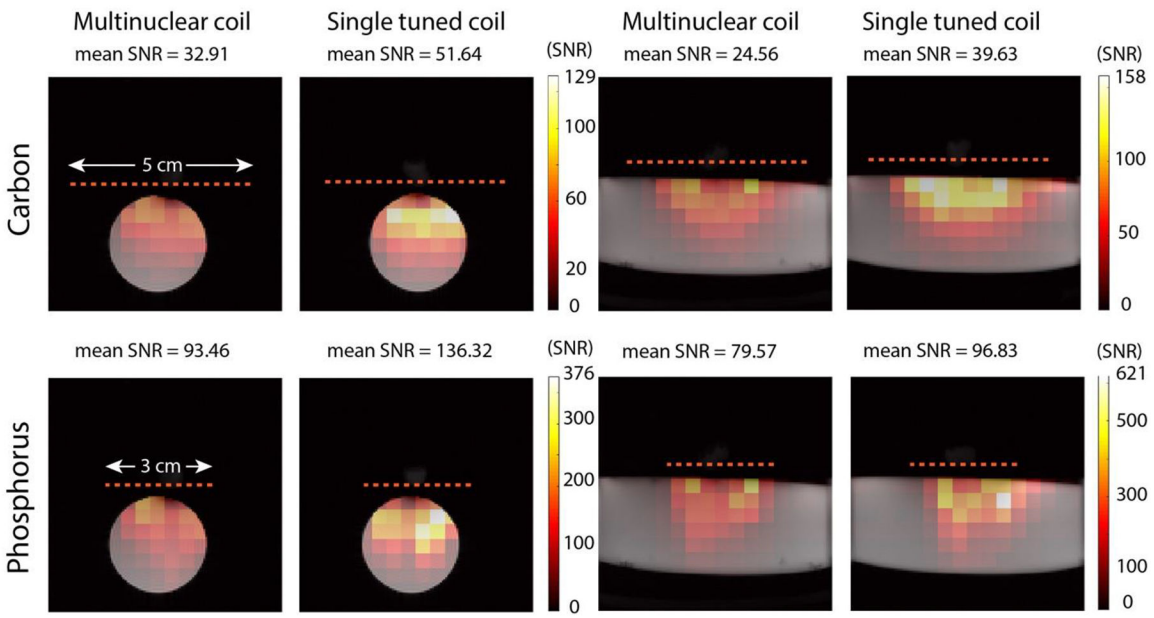

Figure 2:

Signal-to-noise ratio maps for surface coils. The Carbon channel of the multinuclear coil showed a 36.27 % and 38.03 % mean decrease in SNR in the axial and sagittal plane measurements respectively. In the SNR maps, the phosphorus channel of the multinuclear coil showed a 31.44 % and 17.83 % mean decrease in SNR in the axial and sagittal plane respectively. Mean values were calculated over the entire slice. Masks based on the background FLASH images were applied.

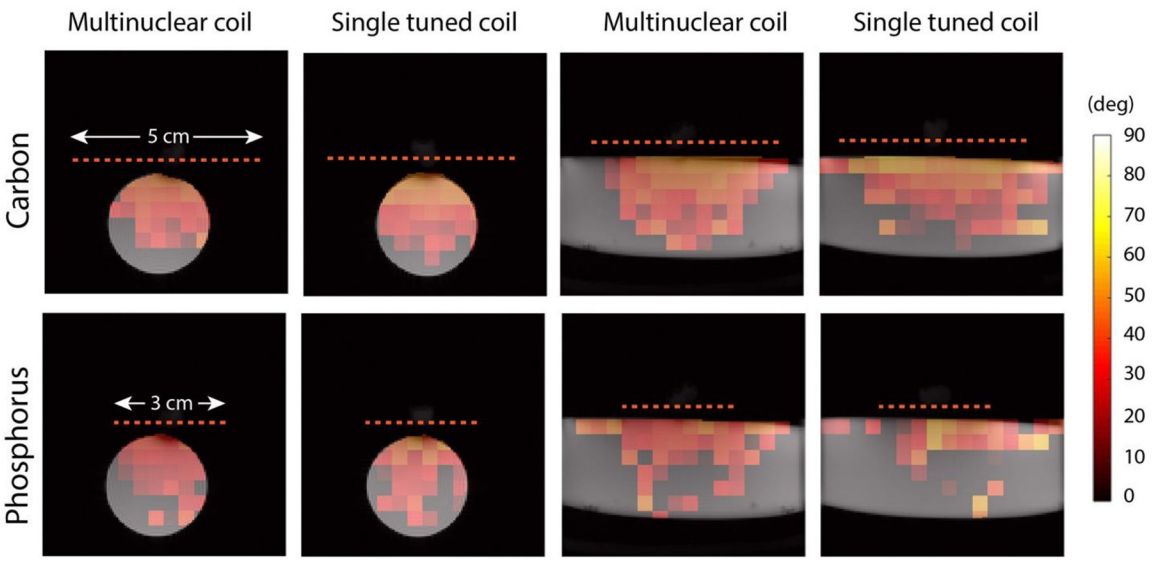

Figure 3:

Flip angle maps for surface coils. Maps calculated using the double angle method with an expected flip angle of 45-degrees. A constant threshold was applied for either carbon or phosphorus coil flip angle maps. Masks based on the background FLASH image were applied to all maps.

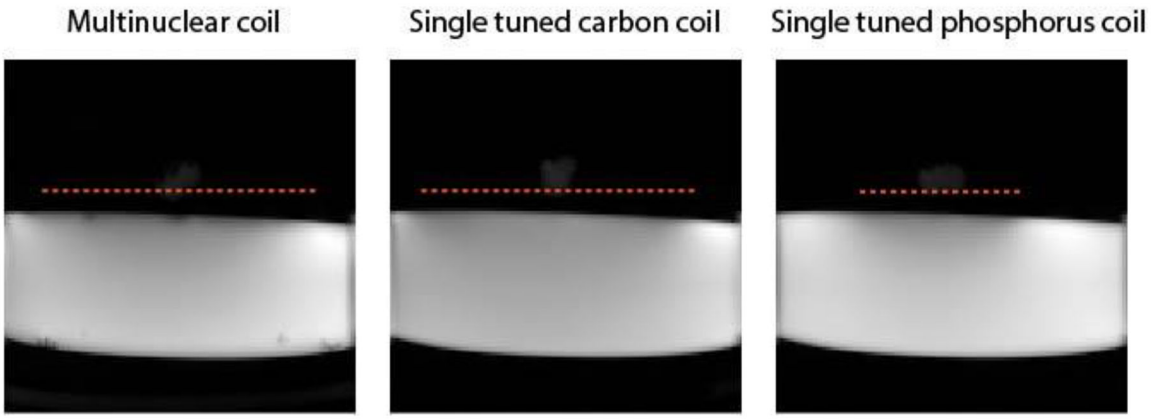

Figure 4:

Proton images in the presence of surface coils. A signal drop in the phantom is visible near the coil elements, which indicates an interaction between the ^{1}H volume coil and the surface coils.

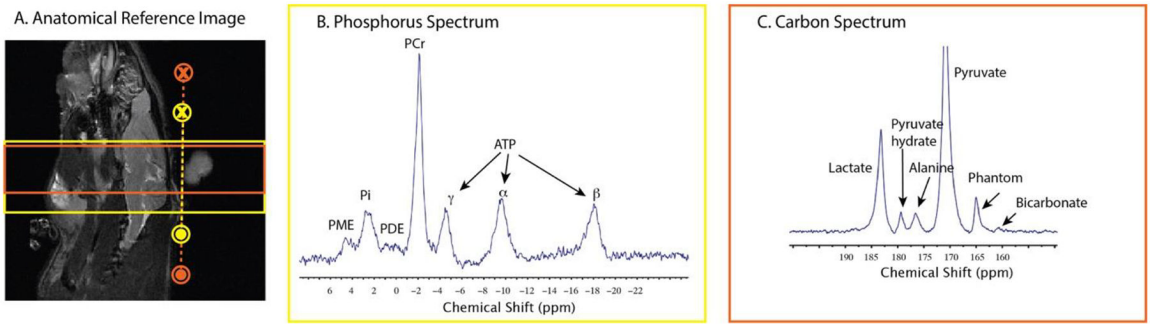

Figure 5:

In vivo carbon and phosphorus spectra. Slice positioning for both carbon (orange) and phosphorus (yellow) acquisitions on a sagittal slice of the head, obtained using a RARE sequence, is shown in A. Phosphorus spectrum (B) shows Phosphomonoesters (PME), inorganic phosphate (Pi), Phosphodiesters (PDE), Phosphocreatine (PCr) and ATP peaks. Carbon spectrum (C) obtained by summing spectra from 18 s to 1 min demonstrate downstream metabolic products of pyruvate namely lactate, alanine, and bicarbonate. A line broadening of 3 Hz was applied for both carbon and phosphorus spectra.

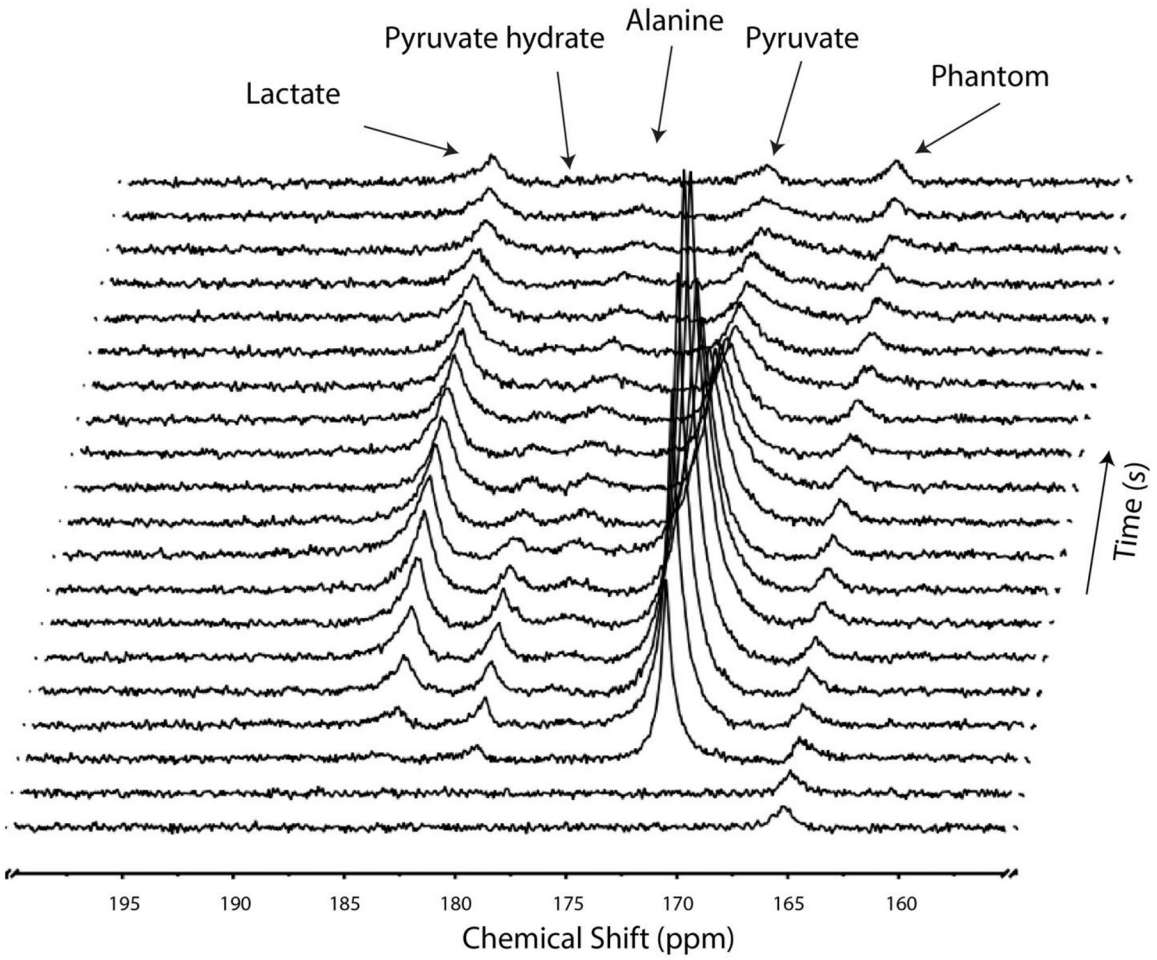

Figure 6:

Dynamic 13C spectra for first 20 time frames (TR = 3s). Lactate and pyruvate hydrate peaks are observed in the initial time frames while alanine appears in later frames.

Table:

Q ratio measurements and SNR efficiency

	Multinuclear coil		**13C channel without LCC trap**	**Single tuned coils**	
	^{13}C channel	**^{31}P channel**	**^{13}C**	**^{13}C**	**^{31}P**
$Q_{unloaded}$	173.93	237.43	278.86	312.51	282.72
Q_{loaded}	130.80	129.61	159.59	166.65	133.92
$Q_{unloaded}/Q_{loaded}$	1.33	1.85	1.75	1.87	2.11
SNR efficiency	0.50	0.68	0.65	0.68	0.73
SNR efficiency w.r.t. single tuned coils	−27.30%	−6.53%	−4.18%	-	-